Proceedings of the ASME 2010 International Design Engineering Technical Conferences & Computers and Information in Engineering Conference
IDETC/CIE 2010
August 15-18, 2010, Montreal, Quebec, Canada

DETC2010-28185

DESIGN OF A LARGE RANGE XY NANOPOSITIONING SYSTEM

Shorya Awtar* and Gaurav Parmar
Precision Systems Design Laboratory
Mechanical Engineering, University of Michigan
Ann Arbor MI 48109

ABSTRACT

Achieving large motion range (> *1 mm*) along with nanometric motion quality (< *10 nm*), simultaneously, has been a key challenge in nanopositioning systems. Practical limitations associated with the individual physical components (flexure bearing, actuators, and sensors) and their integration, particularly in the case of multi-axis systems, have restricted the range of current nanopositioning systems to about *100 μm*. This paper presents a novel physical system layout, with a parallel-kinematic XY flexure mechanism at its heart, that provides a high degree of decoupling between the two motion axes by avoiding geometric over-constraints, provides actuator isolation that allows the use of large-stroke single-axis actuators, and enables a complementary end-point sensing scheme that employs commonly available sensors. These attributes help achieve an unprecedented *10 mm x 10 mm* motion range in the proposed nanopositioning system. Having overcome the physical system design challenges, a dynamic model of proposed nanopositioning system is created and verified via system identification methods. In particular, dynamic non-linearities associated with the large displacements of the flexure mechanism and resulting controls challenges are identified. The physical system is fabricated, assembled, and tested to validate its simultaneous large range and nanometric motion capabilities. Preliminary closed-loop test results, which highlight the potential of this new design configuration, are presented.

1. INTRODUCTION

A nanopositioning system is a mechatronic motion system capable of nanometric motion quality, which is defined in terms of precision (motion repeatability), accuracy (lack of error), and resolution (minimum incremental motion) [1-5]. It comprises a flexure bearing, actuators and drivers, sensors and electronics, and feedback controls implemented on a microcontroller.

Given their high motion quality, nanopositioning systems are vital to several existing and emerging nano-scale microscopy, manipulation, and manufacturing methods [3, 4]. Existing flexure-based nanopositioning systems are capable of *~100 μm* in motion range [6-10], which has adequately served several applications. However, there is now a growing need for multi-axis (most commonly XY) nanopositioning systems that can provide motion range of the order of several millimeters (~ *10 mm x 10 mm*) while maintaining nanometric quality in a compact desktop-size package. Such applications include scanning probe microscopy and metrology [11-15], scanning probe nanolithography [16, 17], memory storage [18], hard-drive fabrication [19], semiconductor fabrication and wafer inspection [20], semiconductor packaging [21], and imaging for stem cell research [22].

One of the key requirements for nanopositioning is the elimination of non-deterministic effects such as friction and backlash, which are commonly seen in bearings and transmissions that rely on rolling or sliding interfaces [23]. In particular, to achieve nanometric precision, it becomes necessary to employ non-contact bearing systems, transmissions, actuators, and sensors.

While mag-lev [24, 25] and aerostatic bearings [26, 27], are able to provide large range and high precision, owing to their non-contact operation, they are sub-optimal for lab-based desktop applications. Mag-lev bearings rely on a sophisticated magnetic circuit that is stabilized via feedback controls. Given their high cost and complexity, these are best suited for niche applications such as wafer-steppers used in high-volume semiconductor fabrication [28]. Air bearings, on the other hand, require a constant supply of clean, high-pressure and low-humidity gas, and are not ideal for vacuum environments [29]. Furthermore, they exhibit small but sustained vibrations (*10-40 nm*) in the bearing direction due to poor damping in the air film [30].

Flexures are the most common bearing choice for desktop-size nanopositioning systems [4-9, 31]. Their monolithic (joint-less) construction entirely eliminates friction and backlash leading to sub-nanometric precision. Additional benefits

*Corresponding Author (awtar@umich.edu, 734-615-0285)

Copyright © 2010 by ASME

include design simplicity, zero maintenance, and potentially infinite life. However, the main drawback of flexure-based nanopositioning systems is that their range has saturated at ~ *100 μm*. This is due to the fact the physical components of the system – bearing, actuators, drivers, sensors, electronics, and control hardware – are now well-matched in their capabilities and have been pushed to their individual maximum performance level [32].

The most common approach to overcome this range limitation is to mount the 'fine' flexure-based nanopositioning system on top of a 'coarse' large-range traditional motion system [13, 14, 20, 22, 33, 34]. While a high motion resolution may be obtained in this fashion, the motion precision of the overall system is still dictated by the coarse stage (*~100 nm*) [35]. Moreover, this arrangement makes the system more complex, bulky, and expensive due to additional physical components and requires more sophisticated control laws.

A desired motion range of *~10 mm* while maintaining a motion quality ~ *1 nm* represents a dynamic range of 10^7, which poses challenge in terms of each of the individual physical components of a flexure-based nanopositioning system. Further design challenges arise from the integration of these physical components, especially in the case of multi-axis systems. Our objective in this paper is to overcome these physical system design challenges and set the stage for control system design, as the first step in achieving large range nanopositioning.

We outline the physical challenges associated with components and system integration in Section 2, and propose a novel physical system concept for a large-range parallel-kinematic XY nanopositioning system that overcomes these challenges in Section 3. Design of experimental hardware, fabrication and assembly, and component specification (mechanical, electromechanical, and electronic) are covered in Section 4. Section 5 presents a lumped-parameter dynamic model of the proposed overall system and its validation via experimental system identification. Section 6 discusses the challenges in controlling this system to meet the various closed-loop dynamic performance requirements, along with our preliminary attempts to address some of these. Open- and closed-loop testing confirms the feasibility of *10 mm x 10 mm* motion range along with nanometric motion quality. The latter is shown to be limited primarily by the controller design. Preliminary close-loop results in Section 7 show single-axis positioning over a *3 mm* range, with less than *4 nm* precision, accuracy, and resolution. Dual-axis positioning is demonstrated by tracing a *5 mm* diameter circle, with a *12.5 nm* positioning resolution but much greater positioning error (*~2 μm*). Potential reasons behind this and other performance limitations are discussed along with plans for future research in Section 8.

2. CHALLENGES IN ACHIEVING LARGE RANGE

Multi-axis nanopositioning systems may be conceived in either a serial [36-38] or parallel [31, 39, 40] kinematic configuration. An XY serial kinematic configuration is simply comprised of two orthogonally arranged single-axis stages, one stacked on top of the other, resulting in an obvious but bulky construction. An XY parallel kinematic configuration is one in which both the X and Y actuators are ground-mounted, which yields a compact layout. This generally results in higher bandwidth due to the lack of moving actuators and greater precision due to the lack of disturbance from moving cables.

Despite these benefits, parallel kinematic configurations are non-obvious in their conception and often exhibit over-constraint. Over-constraint arises from a geometric layout that exhibits coupling between the two motion axes, which ultimately leads to binding and restricts motion range. Systematic constraint-based methods for the conception of XY parallel-kinematic flexure mechanisms that avoid such over-constraint have been reported previously [41, 42]. However, to achieve large range, the design of the nanopositioning system has to incorporate the flexure bearing and the actuators and sensors from the very conception stage. The former cannot be designed in isolation, with actuators and sensors being an after-thought. The individual physical attributes and limitations of these components, described in the following paragraphs, strongly influence large-range nanopositioning capability.

Obviously, the actuator itself has to be capable of large range and nanometric resolution and precision to meet the desired objective. This generally implies the use of direct-drive large-stroke linear actuators that are free of any friction and backlash. One of the most important attributes of such linear actuators is that they generate motion along an 'actuation axis', defined by their geometry, and do not tolerate off-axis loads or displacements. For example, electromagnetic actuators (voice coils and linear motors), which are capable of large range and high resolution and precision, have to be guided along the actuation axis to ensure uniform actuation force. Piezo-electric actuators, e.g. Lead Zirconate Tintanate (PZT) ceramic stacks, provide high motion resolution and precision and may be used in conjunction with displacement amplifiers in large-range nanopositioning. However, any loads acting in directions other than the axis of the brittle ceramic stack cause permanent damage to the actuator. 'Inchworm' style actuators, which are based on a repetitive hold-step-release action provide large range (*>100 mm*) and small step sizes (*~10 nm*), are also common in large range nanopositioning applications [13, 35, 43]. But once again their motion is strictly guided along a specified actuation axis.

Sensing requirements for large-range multi-axis nanopositioning are equally challenging. Given the stringent motion quality requirements, end-point sensing of the moving stage displacements with respect to the reference ground is indispensable. Moreover, multi-axis (XY) motion requires that the sensor for one axis be tolerant of displacements along the other axis. However, most sensors that provide large measurement range and nanometric resolution, e.g. Linear Variable Differential Transducers (LVDT) and linear optical encoders, also have a fixed 'sensing axis' defined by their geometry. These sensors are restricted to measurements along the sensing axis only and are intolerant to any off-axis motion deviations [44]. Capacitance probes, which are capable of nanometric resolution, precision, and accuracy, are unique in

Copyright © 2010 ASME

their ability to tolerate large off-axis displacements, making them highly suitable for multi-axis nanopositioning system. However, their measurement range is typically limited to *10-100 μm*, making them inadequate for large range nanopositioning. Two-axis (XY) optical gratings can provide end-point sensing and large range, while circumventing the off-axis tolerance issue; however, currently available models do not provide a high enough resolution [45]. Finally, while laser interferometry can provide large range, high resolution, and tolerance to off-axis displacements, its use in desktop applications is often impractical, given its size and set-up.

The lack of system-level conceptualization – that considers the flexure bearing, actuator, and sensor in conjunction, and accommodates the limitations of each of these components – is the key reason why large-range nanopositioning has not been accomplished so far. Once a physical system layout that, in principle, is capable of large range and nanometric motion quality has been conceived, control system design to meet specific closed-loop performance can be carried out. We therefore proceed to compile the relevant motion requirements as well as the sensor and actuator limitations that need to be considered in a parallel-kinematic flexure-based XY nanopositioning physical system layout:

I. The two motion axes (X & Y) must be sufficiently decoupled from each other so that motion in one axis does not affect or constrain motion in the other.

II. Parasitic errors along the un-actuated directions (i.e., Z, θ_x, θ_y, and θ_z) should be inherently restricted and minimized via the flexure mechanism kinematics.

III. For each motion axis, the point of actuation on the flexure bearing should move only along the direction of actuation to accommodate the pre-defined actuation axis of large-stroke direct-drive linear actuators.

IV. The layout should be such that the high-resolution large-range multi-axis end-point sensing requirement can be resolved into simpler sensing tasks that are physically realizable using existing high resolution sensors that either provide large range or tolerance to off-axis motions.

3. PROPOSED PHYSICAL SYSTEM DESIGN

To create novel physical system layouts that overcome the above-listed challenges, we propose a deterministic constraint map (Fig. 1) that systematically captures the above desired attributes in a simple graphical manner. This constraint map, comprising rigid stages interconnected by constraint elements, along with sensors and actuators, provides the basis for generating large-range parallel-kinematic XY nanopositioning physical system layouts. Constraint-based design of XY flexure mechanisms has be reported previously [41, 42]. Here we provide an overview, with particular emphasis on sensor and actuator integration.

The constraint map comprises a Motion Stage that is required to have X and Y motions with respect to a Ground. Stage 1 is connected to Ground via Constraint (A), which only allows relative X motion, so as to provide an interface with a ground-mounted large-stroke fixed-axis X-direction linear actuator (e.g. linear motor, voice coil, PZT with motion amplifier, inchworm actuator). To ensure that the X-displacement of Stage 1, generated by the X actuator, is transmitted to the Motion Stage while keeping the latter free to also move in the Y-direction, Stage 1 and Motion Stage are connected via Constraint (C), which only allows relative Y translation between the two. An analogous arrangement is repeated along the Y-direction. Stage 2 is constrained to move only in the Y-direction with respect to Ground due to Constraint (B), and addresses the challenge of integrating a large-stroke Y-direction linear actuator. Further, to transmit this Y motion to the Motion Stage, without affecting or being affected by the latter's X motion, Stage 2 is connected to the Motion Stage via constraint (D), which only allows relative X motion.

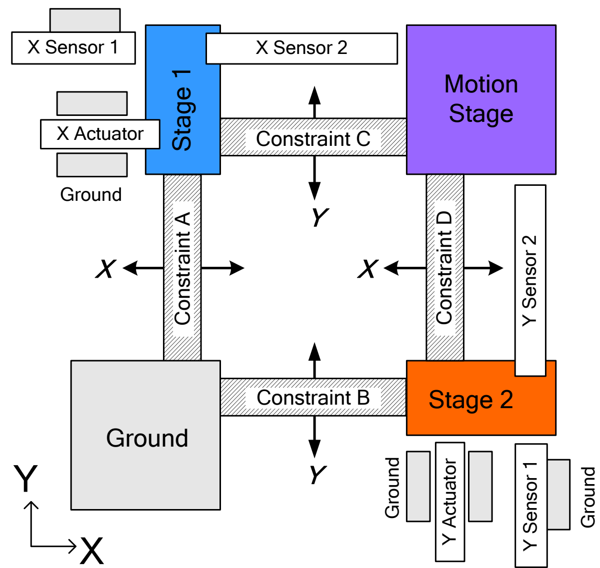

Fig. 1 Proposed Constraint Map

Assuming that the constraint elements (A), (B), (C), and (D) allow relative displacements only in the direction indicated by their respective double-sided arrow, shown in Fig. 1, it may be readily seen that the proposed constraint map can help overcome the physical system layout challenges listed earlier. Since the X and Y motions of the Motion Stage in this parallel-kinematic arrangement are entirely decoupled, large motions along each direction are made possible by eliminating the possibility of geometric over-constraint. Given the inherent properties of the constraint elements, error motion such as in-plane yaw (θ_z) and the three out-of-plane displacements (Z, θ_x, and θ_y) are ideally zero, and very small in practice.

In addition to enabling X actuator integration, Stage 1 also provides an ideal location for mounting a high-resolution, large-stroke, fixed-axis X-direction primary sensor (e.g. linear encoder, LVDT) with respect to Ground. Ideally, the X-displacement of the Stage 1 should be the same as that of the Motion Stage, due to constraint (C). However, in a real implementation, some small relative X-displacement between the Motion Stage and Stage 1 can be expected. This

 Copyright © 2010 ASME

displacement is measured via a second high-resolution X-direction sensor. While the measurement range required of this second sensor is very small, it should be tolerant to the large relative Y-displacement that occurs between Stage 1 and the Motion Stage. Capacitance probes easily meet these requirements. Thus, the proposed constraint map enables large-range high-resolution multi-axis end-point sensing by resolving it into two simpler and practically realizable sensing tasks. A similar dual-sensor arrangement is repeated along the Y-direction.

A practical realization of the proposed constraint map employing the double parallelogram flexure module as constraints (A), (B), (C), and (D), leads to the XY parallel-kinematic physical system shown in Fig. 2. A geometric mirroring, which adds Stages 3 and 4 as well as constraints (A'), (B'), (C'), and (D') to the physical layout, has been carried out without compromising the above arguments. This symmetry helps make the physical system more tolerant to manufacturing errors and thermal fluctuations. The pros and cons of the double parallelogram flexure module as a single- Degree of Freedom (DoF) constraint element and the suitability of the particular embodiment of Fig. 2 over other candidates are discussed in [46, 47]. Sensors and actuators have been intentionally omitted in these illustrations for the sake of clarity.

It is evident that an X actuation at Stage 1 produces only an X-displacement of Stage 1, Stage 3 and the Motion Stage, without perturbing Stages 2 and 4 (Fig. 2A). Similarly, a Y actuation at Stage 2 produces only a Y-displacement of Stage 2, Stage 4 and the Motion stage, without perturbing Stages 1 and 3 (Fig. 2B). When the X and Y forces are applied simultaneously (Fig. 2C), X-displacements only are produced at Stages 1 and 3; Y-displacements only are produced at Stages 2 and 4; and the Motion Stage exhibits both X and Y displacements. The independence between the two axes of actuation, which is a consequence of the constraint layout and design symmetry, ensures large unconstrained motions along both axes. Furthermore, since all the double parallelogram flexure modules offer high stiffness in the in-plane yaw and out-of-plane directions, parasitic error motions are minimized.

The ease of integration of large-stroke fixed-axis linear actuators at Stage 1 and Stage 2 is as expected. Also, it is obvious that a first X sensor (large-range, fixed-axis) can measure the X-displacement of Stage 1 w.r.t. Ground, while a second X sensor (small-range, axis-free) can measure X-displacement of the Motion Stage w.r.t. Stage 1. Y-direction sensing can also be addressed in a similar fashion. (An animation of this physical system concept may be viewed here.)

4. EXPERIMENTAL DESIGN, FABRICATION AND ASSEMBLY

Using previously developed closed-form nonlinear parametric static analysis [41, 47], a detailed design of the XY parallel-kinematic physical system described in the previous section was carried out to achieve a target motion range of *10 mm x 10 mm*. The hardware that was subsequently fabricated and assembled for experimental testing is illustrated in Fig. 3.

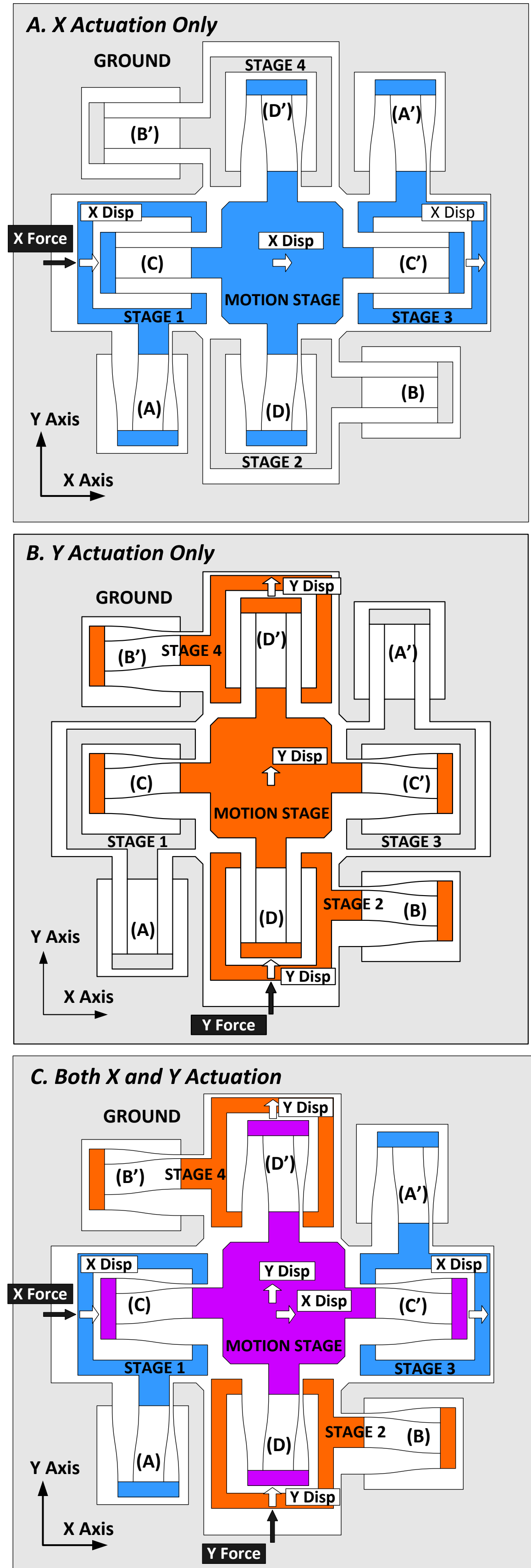

Fig. 2 Physical System Schematic

Copyright © 2010 ASME

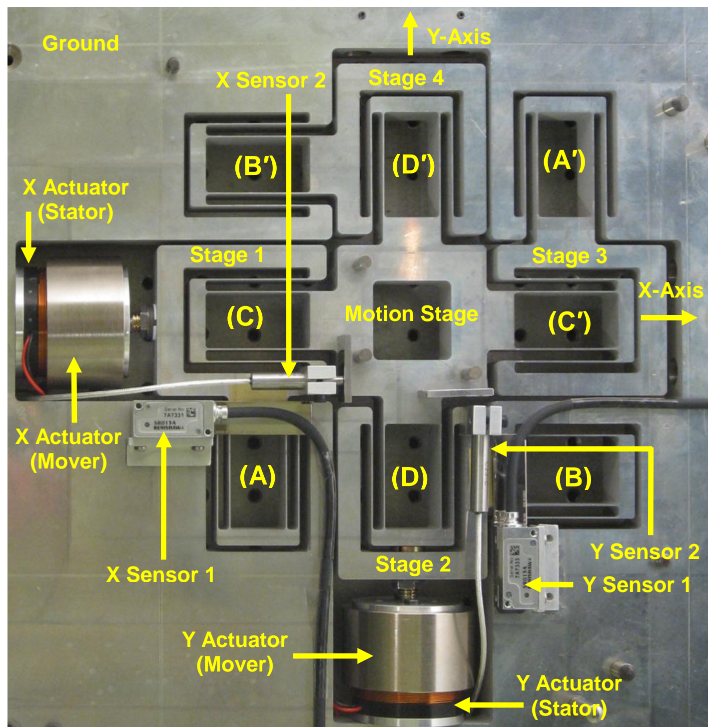

Fig.3 Proposed Large Range XY Nanopositioning System: Proof-of-Concept Prototype

The detailed design process included A. the determination of all relevant dimensions of the flexure bearing, B. materials and manufacturing method selection, C. actuator, driver, sensor, and control hardware specification, and D. ensuring that the entire assembly is free of friction and backlash.

Flexure Bearing: The flexure bearing was sized to minimize in-plane and out-of-plane parasitic error motions as well as cross-axis coupling between the X and Y directions over the motion range of interest. The resulting dimensions are as follows: center to center distance between adjacent double parallelogram flexure modules (DPFM) is *46.25 mm*; beam length is *47.5 mm*; beam in-plane thickness is *0.63 mm*, beam out-of-plane height is *25 mm*; and, inner and outer beam spacing in each DPFM are *12.81 mm* and *18.44 mm*, respectively. The flexure bearing along with the ground frame that is used for mounting all sensors and actuators was created monolithically from a *25.4 mm* thick AL6061-T651 plate, machined down to *25 mm*, using wire- electric discharge machining (EDM). The flexure bearing spans a *255 mm x 255 mm* area in the center, while the outer dimensions of the ground frame (and therefore the overall system) are *385 mm x 385 mm*.

AL6061-T651 was selected as the flexure bearing material because of its good strength-to-modulus ratio, lack of cold-working stresses, long term phase stability, low cost, and ease of availability [41]. Its only drawback is a relatively high coefficient of thermal expansion (CTE), which is mitigated by the geometric design symmetry and therefore deemed acceptable for a proof-of-concept prototype. Wire-EDM is the only practical manufacturing method that produces straight walls over a *25 mm* plate height to yield thin beams and tight tolerances (± *0.005 mm* for the most sensitive dimensions).

The motion characteristics of the flexure bearing by itself were first measured to validate the physical arguments made in the previous section and the closed-form analytical predictions. A *10 mm x 10 mm* motion range capability was demonstrated, along with a cross-axis coupling < *60 μm*, parasitic in-plane rotations < *100 μrad*, and out-of-plane parasitic motions < *4 μm*. These error motion measurements were found to agree with analytically predicted values within *5-10%*, as reported previously [47]. Having characterized and validated the flexure bearing performance, we next present the selection of the actuators, drivers, sensors, and control hardware, and their integration with the flexure bearing.

Sensors and Drivers: As described earlier, the proposed physical system layout enables the decomposition of the large-range nanometric-quality end-point sensing task along each direction into two simpler and practically realizable sensing tasks. For the X-direction, a first sensor is needed to measure the large X-displacement of Stage 1 with respect to Ground. Since Stage 1 is constrained to move along the X-direction only, any fixed-axis non-contact sensor with large range and high resolution can be used. While an LVDT is capable of large range and offers non-contact frictionless operation, its resolution is limited by the Signal to Noise and Distortion Ratio (SINAD) or dynamic range of its drive electronics. SINAD includes both the broad-band noise as well as harmonic distortion that may occur in an electronic circuit [48]. While a 10^7 or *140 dB* dynamic range is required, sensor driver electronics are generally limited to a dynamic range of about *100 dB*.

A linear optical encoder overcomes the above dynamic range limitation because its digital output makes it immune to electronic noise and harmonics. The resolution of a linear encoder is limited simply by its line grating period and electronic interpolation. Therefore, a linear optical encoder (RELM scale, Si-HN-4000 Read-head, and SIGNUM Interface from Renishaw) capable of *5 nm* resolution, *80 mm* measurement range, and *135 mm/s* measurement speed was chosen. The encoder scale is mounted on Stage 1 while the encoder read-head is fixed to the ground, which allows easy routing of the read-head cable.

It was verified experimentally as well as analytically that even though the X-displacements of Stage 1 and the Motion Stage are very close, their relative displacement can be of the order of tens of microns over the entire motion range. This was anticipated in the physical system layout design, and a second X-direction sensor was designated to measure this small displacement in order to achieve end-point sensing. While the measurement range for this task is relatively small, the sensor should be non-contact, high resolution, and tolerant to large Y-displacement of the Motion Stage relative to Stage 1; conditions that are ideally met by a capacitance probe. Accordingly, a probe (Model # C23-C) and driver (CPL290 Elite Series) combination from Lion Precision, capable of

Copyright © 2010 ASME

nanometric resolution over a *50 μm* range at *15 KHz* bandwidth, was selected. The probe was mounted on Stage 1 using a simple flexure-based clamp, while a high precision Starrett gauge block mounted on the Motion Stage serves as the probe target.

The two sensor signals are fed to a micro-controller, where they are added in order to obtain the net X-displacement of the Motion Stage w.r.t. Ground. An analogous arrangement is repeated along the Y-direction. Currently, the resolution of this measurement scheme is limited by the resolution of the optical encoder. This particular encoder model was selected for its relatively lower cost and easy of availability, and was considered acceptable for proof-of-concept prototyping. In the future, we plan to use sub-nm resolution encoders.

Actuators and Drivers: Given the fixed-axis actuator integration capability provided by the proposed physical layout, several actuator options were considered. Despite motion amplification, which adversely affects dynamic performance, PZT actuators are unable to provide the desired motion range. While 'Inchworm' actuators are capable of the necessary range and resolution, their positioning performance is comprised due to impact-induced vibrations even at low speeds [5]. Non-contact direct-drive electromagnetic linear motors are promising but often suffer from magnetic hysteresis and cogging.

Although voice-coil actuators offers sufficiently large non-contact cog-free motion, their resolution, in practice, is limited by the SINAD of it current driver (or amplifier). A current driver, opposed to voltage driver, provides direct control of the actuation force and offers a greater actuation bandwidth. A desired dynamic range of 10^7 or *140 dB* is extremely difficult, if not impossible, to achieve in practical high-current drivers due to the presence of broad-band noise and harmonic distortions. We tested several high-end commercially available linear current amplifiers, which offer considerably lower noise compared switching amplifiers but are still not adequate for our application. The SINAD for LCAM (from Quanser) and Ultimac (from Danaher) linear amplifiers found to be approximately *70 dB*. Instead, a custom built linear amplifier using an ultra-low noise power operational amplifier yielded a SINAD of *90 dB*. Even though this does meet the desired dynamic range, it should be recognized that amplifier noise shows up as an input disturbance in a feed-back control loop, and may be mitigated to some extent via appropriate control design. Based on this systems-level solution for addressing the current amplifier noise (partially via low-noise hardware and partially via feedback control), voice coils prove to be our present best actuator choice for large-range nanopositioning.

Therefore, based on the flexure bearing stiffness characteristics, voice-coil actuators from BEI Kimco Magnetics (model LA24-20-000A) were selected for our application. These actuators have a force constant (K_{act}) of *11.12 N/A* and are capable of *111.2 N* bi-directional peak force. In the proposed physical layout (Fig. 3), since Stage 1 is constrained to move only along the X-axis w.r.t. Ground, the actuator Mover may be directly attached to it. In fact, no additional bearing is needed for the actuator, which provides considerable simplicity in the system integration. In our case, the permanent magnet of the voice-coil actuator is connected to Stage 1 as the Mover, while the coil is attached to the Ground frame as the Stator. This offer two advantages: first, a static coil avoids moving wires, which can be a source of disturbance; and second, the coil, which is a heat source, is separated from the flexure bearing. The Ground frame with its greater thermal mass and surface area is better able to absorb and dissipate this heat generated in the coil due to actuation current. In the future, we plan to carry out careful thermal modeling, and incorporate features in the detailed design that will effectively reject this heat and minimize its affect on the nanopositioning system performance.

The power-amp MP111 from Cirrus Logic MP111 was chosen for our custom-built current amplifier due to its high current capability and *10 μV* root-mean-square (RMS) output noise at *1 MHz* bandwidth. The servo amplifier was designed as an inverting voltage controlled current source (VCCS) in a floating load configuration [49]. The gain (K_{amp}) and the bandwidth of the amplifier were set to be *1 A/V* and *1 kHz*, respectively. The bandwidth is set well above the frequency range of motion control. This amplifier was experimentally tested to show a noise floor of *–120 dB* and harmonic distortion of *–90 dB*.

Real-time Control Hardware: The PXI-8106 real-time controller from National Instruments equipped with PXI-6289 data acquisition card was used to implement the closed-loop control algorithm. The sampling rate was fixed at *5 KHz*.

(A video of the overall experimental hardware assembly and operation may be viewed here.)

5. DYNAMIC MODELING AND SYSTEM IDENTIFICATION

In this section, a dynamic model of the overall nanopositioning system is constructed and validated via experimental system identification, in preparation for control system design. In the frequency range of interest (*~100 Hz*), the system may be modeled as a collection of lumped springs (DPFM) and masses (rigid stages). The DPFM is modeled here as a mass-less spring along both the axial and the transverse directions as shown in Fig. 4. The blue (solid) spring represents the stiffness of the DPFM in its transverse direction and the red (dotted) spring represents its stiffness in its axial direction. The mass of flexure beams and the secondary stage within the DPFM is neglected, in comparison to the mass of the rigid stages. Even though the stiffness of the DPFM in the in-plane yaw and out-of-plane directions is of the same order as the axial stiffness, these other motions are not included in this initial modeling attempt. It is recognized that in-plane rotational and out-of-plane modes will not be captured in the resulting dynamic model, but this assumption provides a degree of simplicity and still offers greater insight into the dynamics and controls of the proposed system.

Copyright © 2010 ASME

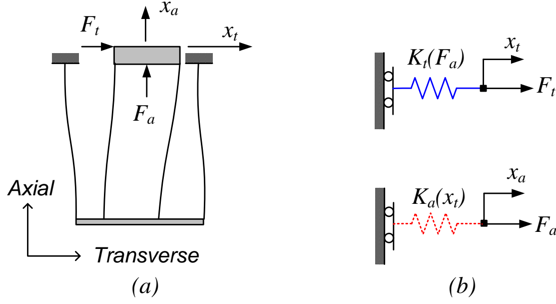

Fig.4 Lumped Spring Model of the Double Parallelogram Flexure Module along its Axial and Transverse Directions

One of the most important consequences of large deformations in flexure mechanisms is the variation of stiffness with loads and displacements. These stiffness variations have been extensively modeled for the DPFM in the past to yield the following closed-form parametric relations [46]:

$$K_t \approx \left[12 - \frac{3}{100}\left(\frac{F_a L^2}{EI}\right)^2\right]\frac{EI}{L^3} \tag{1}$$

$$K_a \approx \frac{1}{\left(T^2 + \frac{9}{25}x_t^2\right)} \cdot \frac{12EI}{L} \tag{2}$$

where E is the young's modulus of the material, and L, T and I denote the length, in-plane beam thickness, and second moment of area, respectively, of the constituent beams within the DPFM. The above relations indicate that the transverse direction stiffness of the DPFM drops quadratically with the axial force (F_a), and its axial direction stiffness has an inverse-quadratic dependence on the transverse displacement (x_t).

Assuming a geometric decoupling between the two axes, a 5 Degree of Freedom (DoF) lumped parameter X-direction model for the proposed nanopositioning system is presented in Fig.5. The X-displacements of the 5 rigid stages in the system define the 5-DoF. Stiffness parameter variation in the X-direction model due to Y-direction force and displacement is incorporated in this model by means of the above stiffness variation relations. An analogous model may be constructed for the Y-direction of the nanopositioning system but is not presented here for the sake of brevity.

The actuator force acting on Stage 1 along the X-direction represents the system input (u_x), and the displacement of the Motion Stage along the X-direction is the output (x_{ms}). The governing equation of motion for the model shown in Fig. 5 can be written as follows:

$$[M]\{\ddot{x}\} + [C_d]\{\dot{x}\} + [K]\{x\} = \{f\}u_x \tag{3}$$

where $\{x\} = [x_1\ x_2\ x_3\ x_4\ x_{ms}]^T$ and $\{f\} = [1\ 0\ 0\ 0\ 0]^T$ are 5×1 displacement and force vectors, respectively. $[M]$, $[C_d]$, and $[K]$ are all $5{\times}5$ symmetric matrices representing mass, damping, and stiffness respectively. The mass and stiffness matrices in this model are as follows:

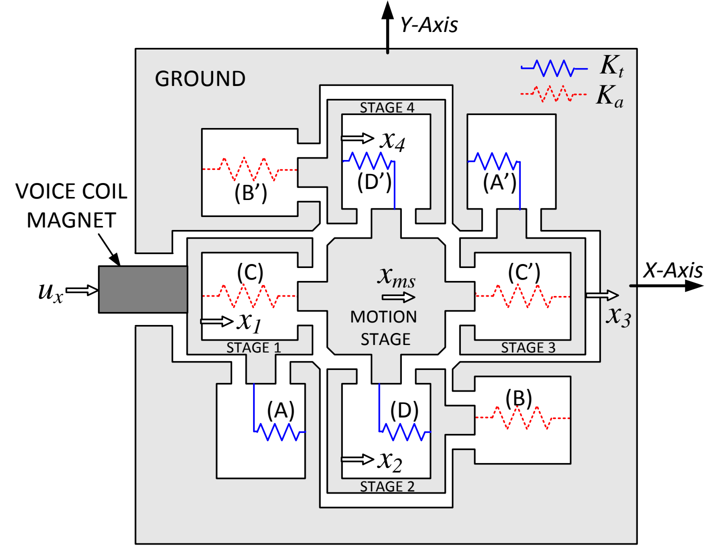

Fig. 5 5-DoF Spring-mass Model of the Nanopositioning System along the X-Direction

$$[M] = \begin{bmatrix} M_{is}+M_{vc} & 0 & 0 & 0 & 0 \\ 0 & M_{is} & 0 & 0 & 0 \\ 0 & 0 & M_{is} & 0 & 0 \\ 0 & 0 & 0 & M_{is} & 0 \\ 0 & 0 & 0 & 0 & M_{ms} \end{bmatrix}$$

$$[K] = \begin{bmatrix} K_t^{(A)}+K_a^{(C)} & 0 & 0 & 0 & -K_a^{(C)} \\ 0 & K_t^{(D)}+K_a^{(B)} & 0 & 0 & -K_t^{(D)} \\ 0 & 0 & K_t^{(A')}+K_a^{(C')} & 0 & -K_a^{(C')} \\ 0 & 0 & 0 & K_t^{(D')}+K_a^{(B')} & -K_t^{(D')} \\ -K_a^{(C)} & -K_t^{(D)} & -K_a^{(C')} & -K_t^{(D')} & \begin{pmatrix} K_t^{(D)}+K_a^{(C)} \\ +K_t^{(D')}+K_a^{(C')} \end{pmatrix} \end{bmatrix}$$

M_{is} = *0.177 Kg* is the mass of Stages 1 through 4, M_{vc} = 0.570 Kg is the mass of the voice coil magnet and M_{ms} = 0.284 Kg is the mass of the Motion Stage. In the stiffness matrix, $K_t^{(A)}$ represents the transverse stiffness of the DPFM (A), and so on. Here, the axial and transverse stiffness of all the DPFM are determined for using Eqs.(1)-(2) for a given Y-direction load or displacement.

To determine the analytical system transfer-function $G_{fx}(s) = X_{ms}(s)/U_x(s)$, a state-space model was derived using Eq.(3), with states $\{z_1\} = \{x\}$ and $\{z_2\} = \{\dot{x}\}$:

$$\begin{bmatrix} \dot{z}_1 \\ \dot{z}_2 \end{bmatrix} = \begin{bmatrix} 0 & I \\ -[M]^{-1}[K] & -[M]^{-1}[C_d] \end{bmatrix}\begin{bmatrix} z_1 \\ z_2 \end{bmatrix} + \begin{bmatrix} 0 \\ [M]^{-1} f \end{bmatrix} u_x$$
$$x_{ms} = [0\ \ 0\ \ 0\ \ 0\ \ 1\ \ 0\ \ 0\ \ 0\ \ 0\ \ 0]\begin{bmatrix} z_1 \\ z_2 \end{bmatrix} \tag{4}$$

Copyright © 2010 ASME

This analytical transfer function is plotted in Fig. 6a, for the nominal X-direction stiffness matrix [*K*] i.e. Y actuation to be zero. The first pole, which occurs at *18 Hz*, represents a rigid body mode in which Stage 1, Motion Stage, and Stage 3 all moves in phase with each other. The next higher mode of interest is at *1315 Hz*, where Motion Stage moves out of phase with respect to Stage 1, demonstrating the non-collocated sensing and actuation in our system. The corresponding pole falls outside the plotted frequency range, and is therefore not seen in Fig. 6a. A similar exercise may be carried out for non-zero Y actuation, which alters the X-direction stiffness matrix [*K*] as per Eqs.(1)-(2). The X-direction transfer function for case of $y_{ms} = 5\ mm$ is plotted in Fig. 6b. It is interesting to note that while there is no significant change in the rigid body mode, which remains at about *18 Hz*, the other mode mentioned above moves from down *1315 Hz* to *150 Hz*.

The above dynamic response predicted by the 5-DOF X-direction model is corroborated experimentally via broadband FFT-based identification techniques using a dynamic signal analyzer (SigLab, Model 20-22A). Here, the experimental set-up consists of the current amplifier, actuator, flexure bearing and the sensor. A band-limited chirp excitation was used within the frequency range of *1Hz* to *500 Hz*. Since the actuator driver is operated in the current mode with a bandwidth of *1 KHz*, both the voice coil actuator and the current amplifier are approximated by constant gains ($K_{act} = 11.12\ N/A$, $K_{amp} = 1.0\ A/V$). This X-direction system identification was carried out for y_{ms} values of *0* and *5 mm*, and the results are plotted in Figs. 6a and 6b, respectively (solid red line). The $G_{fx}(s)$ transfer functions shown here are between the actuator force and Motion Stage displacement. Good agreement between the analytical prediction and experimental measurement is seen for both Y actuation cases. Since damping was not incorporated in the analytical model, it was estimated based on the experimental response.

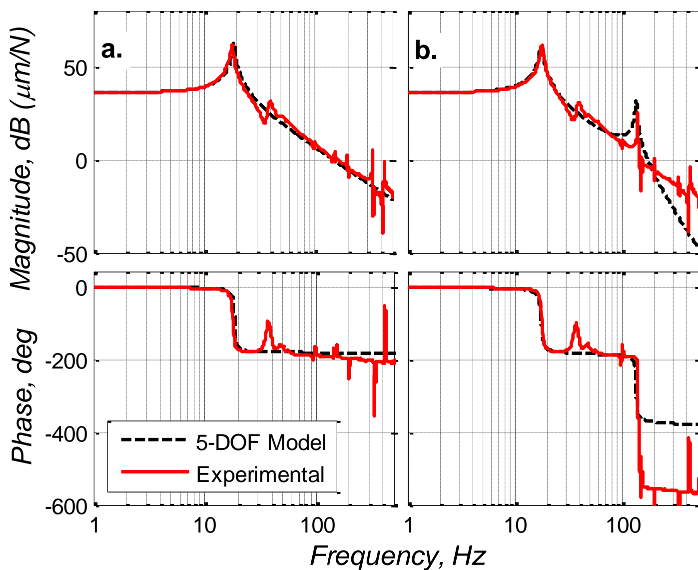

Fig. 6 Comparison between Experimental and Analytical X-Direction Frequency Response: (a.) $y_{ms} = 0$ and (a.) $y_{ms} = 5\ mm$

The critical difference between the transfer functions in Fig. 6a and 6b is observed at *150 Hz*, where the phase drops below *180°* for the operating point in the latter case. Since the 5-DoF model incorporates the variation in X stiffness with Y actuation, it predicts the change in pole location, and thus the early phase loss, quite accurately. The experimental transfer functions show several additional modes, very likely arising from in-plane rotational and out-of-plane dynamics, which were not included in the 5-DoF model. However, despite its simplicity, this model captures all the essential dynamics that are pertinent to Motion Stage position control, up until *150 Hz*, throughout the operating range of motion.

6. CONTROL SYSTEM CHALLENGES AND DESIGN

The performance of a nanopositioning system is specified in terms of its motion precision, accuracy, and resolution, which were defined in Section 1, along with speed of operation. In closed-loop operation, these specifications can be translated to equivalent control system design objectives, as follows:

1. Accuracy and precision depend on command tracking as well as low frequency noise and disturbance rejection.

2. Positioning noise and the minimum incremental motion determine the resolution. While positioning noise depends on high frequency noise and disturbance rejection, minimum incremental motion is determined by command tracking.

3. Closed-loop bandwidth determines the speed and response time of the nanopositioning system

4. Closed-loop robustness against modeling uncertainties and parameter variations affect all of the above.

In the context of our physical system, several control design challenges and trade-offs were identified in achieving the above performance objectives:

1. Most existing nanopositioning systems have a high first natural frequency because they operate over a relatively small motion range. Therefore, simple lower-order controllers with integrators (e.g., PI, PII) provide good overall performance [5]. In our case, the extended range of motion is a consequence of low primary stiffness, which also leads to a low first natural frequency (*~18 Hz*). In order to achieve a bandwidth greater than this first natural frequency, a higher-order controller is needed, which poses greater performance trade-offs, particularly in terms of bandwidth and noise rejection.

2. In general, lightly damped poles and zeros of in a flexible system severely affect the closed loop stability and performance [50]. In addition to this, the non-collocation of sensor and the actuator in our case leads to additional challenges in terms of achievable bandwidth [51].

3. As mentioned in Section 5, the parameter variation due to coupled dynamics between the two axes, and resulting variations in the frequency response along each axis, poses further challenges in obtaining robust stability and performance.

4. Various sources of noise and disturbance in our system limit the achievable resolution. This includes feedback sensor noise, actuator driver noise, electronic noise in the data acquisition hardware, and last but not the least, mechanical floor

Copyright © 2010 ASME

vibrations. The individual contribution of these sources to the positioning noise will depend upon their respective magnitude, where they enter the system, the control architecture, and the controller design (Fig. 7).

In additional to these challenges that are specific to our physical system, any closed-loop framework in general has its own set of fundamental limitations and trade-offs [52, 53]. One such trade-off pertinent to our case (between amplifier noise rejection and robustness) is discussed in further detail later in this section.

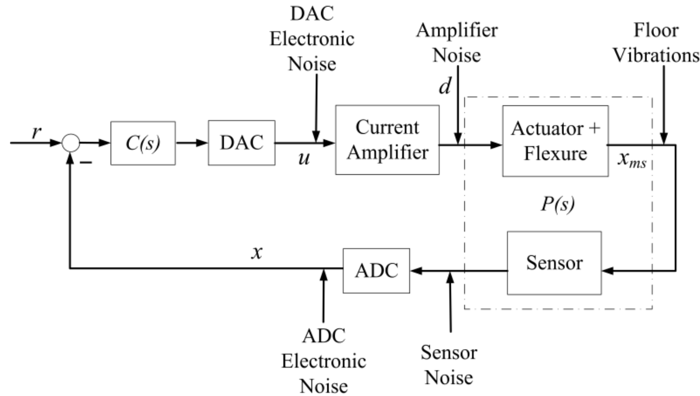

Fig.7 Control Architecture implemented along each axis

Although we have identified various control system objectives, challenges and limitations, our objective in this paper is to attempt a preliminary control system design that can demonstrate large range nanopositioning capability at a low bandwidth. While parameter variation due to coupled dynamics has been recognized in the modeling above, its effect was found to be negligible in the low frequency range ($< 150\ Hz$). Therefore, we propose to implement identical but independent control schemes for each axis, as shown in Fig.7. Here, the voice coil actuator, the flexure bearing, and the sensor altogether are denoted by $G_{xx}(s)$, which is the same as $K_{act}*G_{fx}(s)$), assuming no sensor dynamics. The controller is represented by $C(s)$. The close-loop command is r, amplifier noise is d, actual Motion Stage displacement is x_{ms}, and measured displacement is x.

The transfer function derived from the 5-DOF model in Eq.(4), may be stated as follows:

$$G_{xx}(s) = 2.45\times 10^{11}\frac{\left(s^2 + 7672s + 1.507\times 10^7\right)}{\left(s^2 + 6.82s + 1.22\times 10^4\right)}\times \frac{1}{\left(s^2 + 24.05s + 7.12\times 10^5\right)\left(s^2 + 5491s + 7.73\times 10^6\right)} \quad (5)$$

This open-loop transfer function is used design a lag-lead controller, $C(s)$, to achieve acceptable closed-loop stability and performance. The lag part includes an integrator to achieve zero steady state error and the lead part is needed to increase the phase near gain crossover frequency. In order to ensure a good roll-off at higher frequencies, an additional pole is added after the crossover frequency. Upon a few iterations, the following feedback controller was implemented:

$$C(s) = 170\frac{(s+30)(s+71)}{s(s+1150)(s+2515)} \quad (6)$$

The experimentally measured frequency response of the resulting loop transfer function $L(s) = G_{xx}(s)C(s)$ along with corresponding stability margins is shown in Fig. 8. This confirms a Gain Margin or $12.9\ dB$ and a Phase Margin of 37.2^o. Fig. 9 shows the experimentally obtained frequency response of the closed loop transfer functions from r to x. The dip in gain and phase seen at lower frequencies is due to the zeros of the $C(s)$. This dip in magnitude as well as phase, albeit small, can affect command tracking when positioning accuracy is critical.

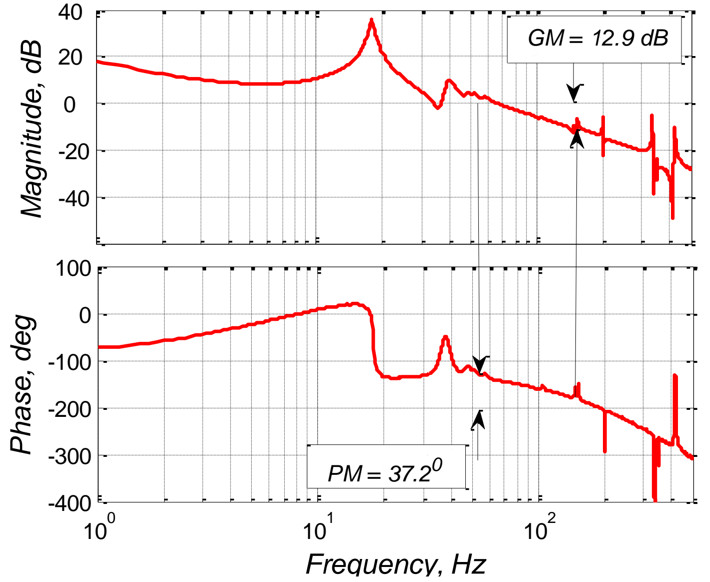

Fig.8 Experimentally Measured Frequency Response of the Loop Transfer Function, L(s)

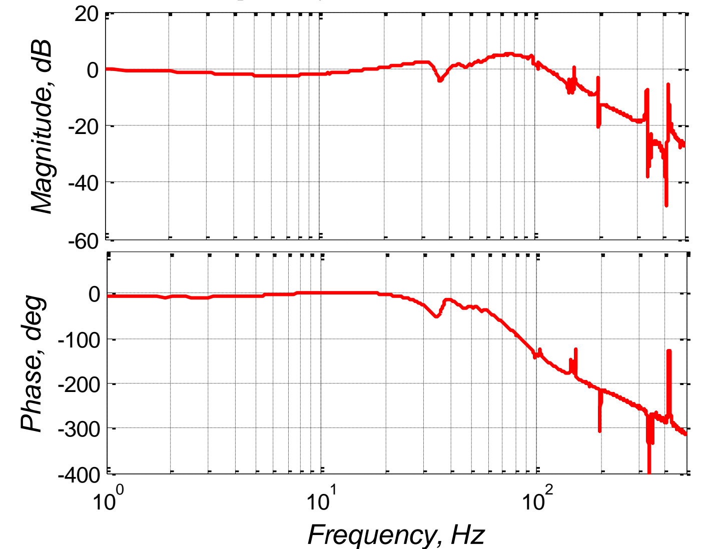

Fig. 9 Experimentally Measured Frequency Response of the Closed-loop Transfer Function

Copyright © 2010 ASME

As mentioned earlier, the noise in the voice coil amplifier proves to be a major limiting factor in achieving nanometric resolution. Therefore, it is important to consider the affect of the feedback controller on the contribution of this noise to positioning resolution. The amplifier noise can be thought of as input disturbance acting on the plant, as shown in Fig. 7. The closed-loop transfer function from *d* to *x* is given by:

$$T_{dx}(s) = \frac{G_{xx}(s)}{1 + C(s)G_{xx}(s)} \tag{7}$$

In the open-loop configuration, $T_{dx}(s)$ is simply equal to $G_{xx}(s)$. Hence, the ability of the closed-loop system to reject this noise depends upon the magnitude of $C(s)$. In other words, higher the closed-loop bandwidth, which requires a high $C(s)$ over a certain frequency range, also ensures improved amplifier noise rejection. However, there is obviously a limit to which $C(s)$ can be increased due to concerns arising from stability margins and sensor noise amplification.

Assuming the amplifier noise to be Gaussian white noise, its contribution is directly proportional to the area under the transfer function $T_{dx}(s)$ [10]. Fig. 10 shows the comparison between the open-loop and closed-loop transfer functions $G_{xx}(s)$ and $T_{dx}(s)$, from *d* to *x*, for the controller given in Eq.(6). The area under the transfer function $T_{dx}(s)$ is *4* times less than the area under the transfer function $G_{xx}(s)$, which qualitatively indicates a corresponding improvement in amplifier noise rejection. To measure the positioning noise, the stage was commanded to stay at a fixed position. Fig. 11 shows the probability distribution of the open-loop and closed-loop positioning noise (X-displacement of the Motion Stage) as measured by the sensors along X-axis. The sampling frequency was fixed at *5 KHz*. The closed-loop positioning noise, which is also a measure of the resolution, is less than *4 nm* RMS. This is *3.6* times better than what is measured in the open-loop, also shown in Fig. 11.

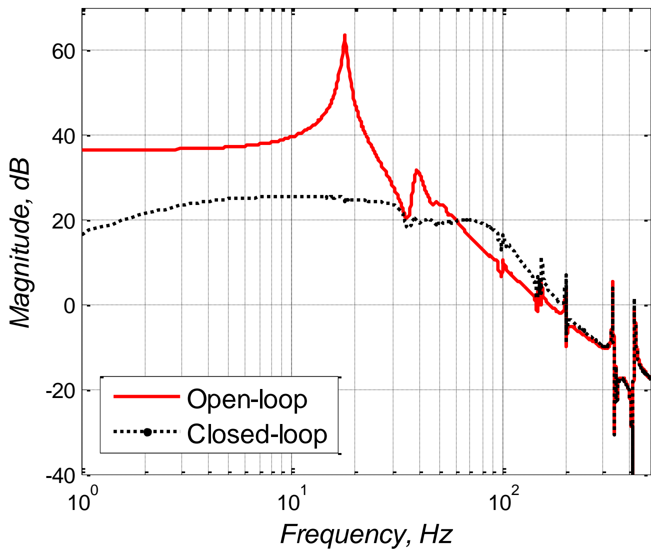

Fig. 10 Experimentally Measured Transfer Function from Amplifier Noise to Motion Stage Position

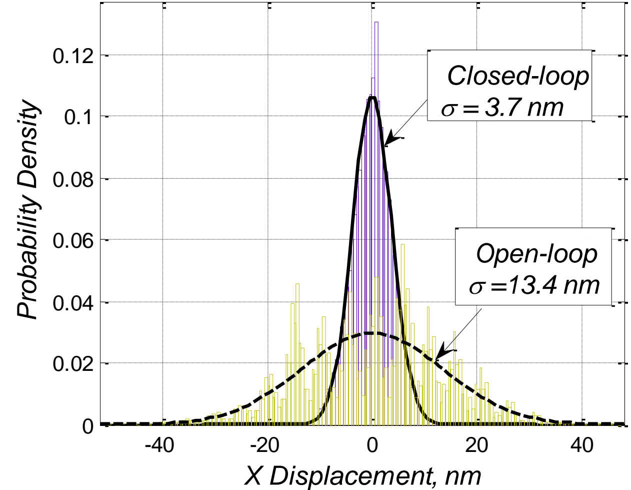

Fig. 11 Amplitude Distribution of the Open-loop and Closed-loop Positioning Noise

7. PRELIMINARY CLOSED LOOP RESULTS AND DISCUSSION

In this section, we present some preliminary closed-loop performance plots for the proposed XY nanopositioning system based on the controller design discussed above. Fig.12 shows the position response of the Motion Stage to step commands of size *500 μm* and *20 nm* (inset) along the X-axis, over a 3mm range. The steady state positioning resolution as seen in this time-domain plot is under *4 nm* RMS, in agreement with Fig.11. This figure also indicates a positioning precision and accuracy of the order of the positioning resolution. Even though the physical system is capable of motion range well above 3mm, our testing was limited due to a previously unrecognized current limit on the actuator amplifier. We are in the process of upgrading this amplifier to be able repeat this *500 μm* step test for ranges as large as 10mm.

Next, the Motion Stage was commanded to move in a *5 mm* diameter circle at *1 Hz*. This was done by sending sinusoidal reference commands along both the axes with a magnitude of *2.5 mm* and separated in phase by 90^0. A relatively large deviation of the actual path of the Motion Stage from the reference circle was observed. A least square ellipse was fitted to the actual path reveals a maximum trajectory deviation of approximately *2.25 μm*. The positioning noise w.r.t. the fitted ellipse was measured to be less than *12 nm* RMS. Fig. 13 shows the measured position response of the Motion Stage along with the least square fit ellipse. For better visualization, the error from the least square fit ellipse is magnified *5000* times.

Even though the positioning noise and therefore resolution (*12 nm* RMS) is reasonable, the trajectory tracking error (or lack of positioning accuracy) is considerably large, especially when compared to the above single axis positioning results. This error is a consequence of the fact that over a motion range of several millimeters, even a small difference in the actual phase of the two axes leads to a pronounced deviation from the command trajectory.

Copyright © 2010 ASME

One of the reasons why command tracking in the two-axis control case suffers is that we have had to reduce the controller gain to avoid an unexpected instability. We believe that this instability, not seen in the single-axis case, arises from a cross-axis coupling dynamics that was ignored in the modeling and controller design. To address this issue, we are considering several options, which includes: 1. Modeling the system as a Multi-Input Multi-Output system to capture the pertinent cross-axis coupling dynamics and design a controller accordingly, 2. Consider the use of passive damping schemes that might suppress this cross-axis coupling dynamics, and 3. Consider the use of pre-filters to improve the command tracking without the need for increasing feedback controller gains.

Fig. 12 Motion Stage Position Response for 1 mm steps and 20 nm steps along X-axis

Fig. 13 Motion Stage tracking a 5 mm diameter circle

8. CONCLUSION

In this paper, we have presented a novel physical layout that holds the potential for achieving the goal of large-range multi-axis nanopositioning. Meeting this objective has been a long-standing challenge because of limitations posed by individual nanopositioning components as well as their integration. These limiting attributes of bearings, sensors, and actuators in nanopositioning have been identified and highlighted. Based on this understanding, we have employed a systematic constraint-based design approach to generate an XY parallel-kinematic flexure-based physical system layout that ensures a high degree of geometric decoupling between the two motion axes, provides actuator isolation that allows the use of large-stroke single-axis actuators, and enables a complementary end-point sensing scheme that employs commonly available sensors.

The proposed physical system has been fabricated and assembled, and shown to be simultaneously capable of large range and high motion quality, in principle, due to a lack of friction and backlash anywhere in the assembly. We have also presented some preliminary dynamic modeling of this physical system, followed by a basic controller design. While preliminary closed-loop results provide a promising start, this exercise reveals the considerable challenges and trade-offs in the control system design associated with the proposed physical system. Although a physical system that is inherently capable of large range and nanometric motion quality is a necessary first step towards achieving large range nanopositioning, it is clear that motion quality ultimately depends on the closed-loop performance (command tracking, noise and disturbance rejection, bandwidth, and robustness) provided by the control system. We are currently working on addressing these challenges and ultimately hope to refine the physical system design accordingly.

REFERENCES

[1] Hicks, T. R., and Atherton, P. D., 1997, *The Nanopositioning Book*, Queensgate Instruments Ltd.
[2] Sato, K., 2006, "Trend of Precision Positioning Technology," Proc. ABCM Symposium Series in Mechatronics, 2, pp. 739-750.
[3] Jordan, S., and Lula, B., 2005, "Nanopositioning: The Technology and the Options," The 2005 Photonics Handbook.
[4] Application Note: Nanopositioning Tools and Techniques for R&D Applications, nPoint Inc.
[5] Devasia, S., Eleftheriou, E., and Moheimani, S. O. R., 2007, "A Survey of Control Issues in Nanopositioning," IEEE Transactions on Control Systems Technology, 15(5), pp. 802-23.
[6] Product Model # NPS-XY-100A, Queensgate Instruments
[7] Product Model # P-541.2, Piezo XY Nanopositioning Stage, PhysikInstrumente
[8] Product Model # NanoBio2200, Mad City Labs
[9] Product Model # PXY400, PiezoSystem Jena

Copyright © 2010 ASME

[10] Aphale, S. S., Bhikkaji, B., and Moheimani, S. O. R., 2008, "Minimizing scanning errors in piezoelectric stack-actuated nanopositioning platforms," IEEE Transactions on Nanotechnology, 7(1), pp. 79-90.
[11] Dai, G., Pohlenz, F., Danzebrink, H.-U., Xu, M., Hasche, K., and Wilkening, G., 2004, "Metrological large range scanning probe microscope," Review of Scientific Instruments, 75(4), pp. 962-969.
[12] Hausotte, T., Jaeger, G., Manske, E., Hofmann, N., and Dorozhovets, N., 2005, "Application of a Positioning and Measuring Machine for Metrological Long-range Scanning Force Microscopy," Proc. SPIE, San Diego, CA, 5878(2), pp. 1-12.
[13] Kramar, J. A., 2005, "Nanometre Resolution Metrology with the Molecular Measuring Machine," Measurement Science & Technology, 16(11), pp. 2121-28.
[14] Sinno, A., Ruaux, P., Chassagne, L., Topcu, S., and Alayli, Y., 2007, "Enlarged Atomic Force Microscopy Scanning Scope: Novel Sample-holder Device with Millimeter Range," Review of Scientific Instruments, 78(9), pp. 1-7.
[15] Weckenmann, A., and Hoffmann, J., 2007, "Long Range 3 D Scanning Tunnelling Microscopy," CIRP Annals - Manufacturing Technology, 56(1), pp. 525-528.
[16] Salaita, K., Wang, Y. H., and Mirkin, C. A., 2007, "Applications of Dip-Pen Nanolithography," Nature Nanotechnology, 2(3), pp. 145-55.
[17] Mirkin, C. A., 2001, "Dip-Pen Nanolithography: Automated Fabrication of Custom Multicomponent, Sub-100-Nanometer Surface Architectures," MRS Bulletin, 26(7), pp. 535-538.
[18] Sebastian, A., Pantazi, A., Pozidis, H., and Eleftheriou, E., 2008, "Nanopositioning for probe-based data storage [Applications of Control]," IEEE Control Systems Magazine, 28(4), pp. 26-35.
[19] Van De Moosdijk, M., Van Den Brink, E., Simon, K., Friz, A., Phillipps, G., Travers, R., and Raaymakers, E., 2002, "Collinearity and stitching performance on an ASML stepper," Proc. SPIE, Santa Clara, CA, 4688(1-2), pp. 858-66.
[20] Hongzhong, L., Bingheng, L., Yucheng, D., Yiping, T., and Dichen, L., 2003, "A motor-piezo actuator for nano-scale positioning based on dual servo loop and nonlinearity compensation," Journal of Micromechanics and Microengineering, 13(2), pp. 295-9.
[21] Han, D., and Zhenhua, X., 2006, "Motion stages for electronic packaging design and control," IEEE Robotics & Automation Magazine, 13(4), pp. 51-61.
[22] O'brien, W., 2005, "Long-range motion with nanometer precision," Photonics Spectra, 39
[23] Slocum, A. H., 1992, *Precision Machine Design*, Society of Manufacturing Engineers.
[24] Kim, W.-J., Verma, S., and Shakir, H., 2007, "Design and precision construction of novel magnetic-levitation-based multi-axis nanoscale positioning systems," Precision Engineering, 31(4), pp. 337-350.
[25] Holmes, M., Hocken, R., and Trumper, D., 2000, "The long-range scanning stage: a novel platform for scanned-probe microscopy," Precision Engineering, 24(3), pp. 191-209.
[26] Maeda, G. J., Sato, K., Hashizume, H., and Shinshi, T., 2006, "Control of an XY nano-positioning table for a compact nano-machine tool," JSME International Journal, Series C (Mechanical Systems, Machine Elements and Manufacturing), 49(1), pp. 21-7.
[27] Dejima, S., Gao, W., Katakura, K., Kiyono, S., and Tomita, Y., 2005, "Dynamic modeling, controller design and experimental validation of a planar motion stage for precision positioning," Precision Engineering, 29(3), pp. 263-271.
[28] Resor, G., 2009, "SPIE tracks the tightening litho horse race," Solid State Technology, March Issue
[29] Bisschops, T., and Vijfvinkel, J., 2001, "Large ultra-precision motion feedthrough designs," Vacuum, 60(1-2), pp. 161-5.
[30] Manske, E., Hausotte, T., Mastylo, R., Hofmann, N., and Jager, G., 2005, "Nanopositioning and Nanomeasuring Machine for high accuracy measuring procedures of small features in large areas," Proc. SPIE, Jena, Germany, 5965(9), pp. 1-11.
[31] Culpepper, M. L., and Anderson, G., 2004, "Design of a low-cost nano-manipulator which utilizes a monolithic, spatial compliant mechanism," Precision Engineering, 28(4), pp. 469-482.
[32] Schitter, G., 2008, "Scanning probe microscopy at video-rate," Materials Today, 11(1)
[33] Choi, Y.-M., Kim, J. J., Kim, J., and Gweon, D.-G., 2008, "Design and control of a nanoprecision XY Theta scanner," Review of Scientific Instruments, 79(4), pp. 045109-7.
[34] Pahk, H. J., Lee, D. S., and Park, J. H., 2001, "Ultra precision positioning system for servo motor-piezo actuator using the dual servo loop and digital filter implementation," International Journal of Machine Tools and Manufacture, 41(1), pp. 51-63.
[35] Zhelyaskov, V., Broderick, M., Raphalovitz, A., and Davies, B., 2006, "Automated piezoelectric nanopositioning systems - Long travel ranges and accurate angular movement create new opportunities in biomedical manipulation systems," IEEE Circuits and Devices Magazine, 22
[36] Fischer, F. L., 1981, Symmetrical 3 DOF Compliance Structure, US Patent 4,447,048
[37] Smith, A. R., Gwo, S., and Shih, C. K., 1994, "A new high resolution two-dimensional micropositioning device for scanning probe microscopy," Review of Scientific Instruments, 64(10), pp. 3216-3219.
[38] Dagalakis, N. G., Kramer, J. A., Amatucci, E., and Bunch, R., 2001, "Kinematic Modelling and Analysis of Planer Micro-positioner," Proc. ASPE 16th Annual Meeting, pp. 135-138.
[39] Yao, Q., Dong, J., and Ferreira, P. M., 2007, "Design, analysis, fabrication and testing of a parallel-kinematic micropositioning XY stage," International Journal of Machine Tools and Manufacture, 47(6), pp. 946-961.
[40] Chen, K. S., Trumper, D. L., and Smith, S. T., 2002, "Design and control for an electromagnetically driven X-Y-[theta] stage," Precision Engineering, 26(4), pp. 355-369.

 Copyright © 2010 ASME

[41] Awtar, S., 2004, "Analysis and Synthesis of Planer Kinematic XY Mechanisms," Sc.D. Thesis, Massachusetts Institute of Technology, Cambridge MA.
[42] Awtar, S., and Slocum, A. H., 2005, "Topology Evolution of High Performance XY Flexure Stages," Proc. ASPE Annual Meeting, Norfolk, VA, Paper # 1802
[43] Klocke, V., 2002, "Engineering in the nanocosmos: Nanorobotics moves kilograms of mass," Journal of Nanoscience and Nanotechnology, 2(3-4), pp. 435-40.
[44] Gao, W., Dejima, S., Yanai, H., Katakura, K., Kiyono, S., and Tomita, Y., 2004, "A surface motor-driven planar motion stage integrated with an XY[theta]Z surface encoder for precision positioning," Precision Engineering, 28(3), pp. 329-337.
[45] Product # NanoGrid Planar Encoder System: Model A, Optra Inc.
[46] Awtar, S., Slocum, A. H., and Sevincer, E., 2007, "Characteristics of Beam-based Flexure Modules," ASME Journal of Mechanical Design, 129(6), pp. 625-639.
[47] Awtar, S., and Slocum, A. H., 2007, "Constraint-based Design of Parallel Kinematic XY Flexure Mechanisms," ASME Journal of Mechanical Design, 129(8), pp. 816-830.
[48] Rapuano, S., Daponte, P., Balestrieri, E., De Vito, L., Tilden, S. J., Max, S., and Blair, J., 2005, "ADC parameters and characteristics - Part 6 in a series of tutorials in instrumentation and measurement," IEEE Instrumentation and Measurement Magazine, 8(5), pp. 44-54.
[49] Application Note 13: Voltage to Current Conversion
[50] Book, W. J., 1993, "Controlled motion in an elastic world," Transactions of the ASME. Journal of Dynamic Systems, Measurement and Control, 115(2B), pp. 252-61.
[51] Spector, V. A., and Flashner, H., 1990, "Modeling and design implications of noncollocated control in flexible systems," Transactions of the ASME. Journal of Dynamic Systems, Measurement and Control, 112(2), pp. 186-93.
[52] Lee, C., and Salapaka, S. M., 2009, "Two degree of freedom control for nanopositioning systems: fundamental limitations, control design, and related trade-offs," Proc. American Controls Conference, Piscataway, NJ, pp. 1664-9.
[53] Skogestad, S., and Postlethwaite, I., 2005, *Multivariable Feedback Control, Analysis and Design*, Wiley, New York.

Copyright © 2010 ASME